Process-Oriented Diagnosis of East Pacific Warm Pool Intraseasonal Variability

ERIC D. MALONEY

Department of Atmospheric Science, Colorado State University, Fort Collins, Colorado

XIANAN JIANG

Joint Institute for Regional Earth System Science and Engineering, University of California, Los Angeles, Los Angeles, California

SHANG-PING XIE

Scripps Institution of Oceanography, University of California, San Diego, La Jolla, California

JAMES J. BENEDICT

Earth Sciences Division, Lawrence Berkeley National Laboratory, Berkeley, California

(Manuscript received 10 January 2014, in final form 13 May 2014)

ABSTRACT

June–October east Pacific warm pool intraseasonal variability (ISV) is assessed in eight atmospheric general circulation simulations. Complex empirical orthogonal function analysis is used to document the leading mode of 30–90-day precipitation variability in the models and Tropical Rainfall Measuring Mission observations. The models exhibit a large spread in amplitude of the leading mode about the observed amplitude. Little relationship is demonstrated between the amplitude of the leading mode and the ability of models to simulate observed north-northeastward propagation.

Several process-oriented diagnostics are explored that attempt to distinguish why some models produce superior ISV. A diagnostic based on the difference in 500–850-hPa averaged relative humidity between the top 5% and the bottom 10% of precipitation events exhibits a significant correlation with leading mode amplitude. Diagnostics based on the vertically integrated moist entropy budget also demonstrate success at discriminating models with strong and weak variability. In particular, the vertical component of gross moist stability exhibits a correlation with amplitude of −0.9, suggesting that models in which convection and associated divergent circulations are less efficient at discharging moisture from the column are better able to sustain strong ISV.

Several other diagnostics are tested that show no significant relationship with leading mode amplitude, including the warm pool mean surface zonal wind, the strength of surface flux feedbacks, and 500–850-hPa averaged relative humidity for the top 1% of rainfall events. Vertical zonal wind shear and 850-hPa zonal wind do not appear to be good predictors of model success at simulating the observed northward propagation pattern.

1. Introduction

Intraseasonal variability (ISV) in the east Pacific warm pool during boreal summer has become an increasing research focus over the last decade (Maloney and Hartmann 2000a; Maloney and Esbensen 2003; Barlow and Salstein 2006; Jiang and Waliser 2008; Maloney et al. 2008; Lin et al. 2008; Small et al. 2011; Van Roekel and Maloney 2012; Jiang et al. 2012; Rydbeck et al. 2013; Jiang et al. 2013). Significant spectral peaks near 50-day period can be found in this region in many variables including SST, convective indices, and winds (Maloney and Esbensen 2003; Maloney et al. 2008). Previous studies also documented the presence of a biweekly intraseasonal mode in the east Pacific (e.g., Jiang and Waliser 2009; Wen et al. 2011; Jiang et al. 2012), although we will confine our discussion of ISV in this

Corresponding author address: Eric D. Maloney, Department of Atmospheric Science, Colorado State University, 1371 Campus Delivery, Fort Collins, CO 80523-1371.
E-mail: emaloney@atmos.colostate.edu

DOI: 10.1175/JCLI-D-14-00053.1

paper to time scales of 30–90 days. ISV in this region is characterized by enhanced convection in the east Pacific warm pool to the east of 120°W that is accompanied by anomalous low-level westerly flow, alternating with suppressed convective periods accompanied by anomalous easterlies (Maloney and Esbensen 2003; Jiang et al. 2013). Tropical cyclone activity in the east Pacific, Gulf of Mexico, and Caribbean Sea is enhanced when ISV is in its convectively active phase (Maloney and Hartmann 2000a,b). Similar to the monsoon system of South Asia, northward propagation of intraseasonal precipitation and wind anomalies is prominent in the east Pacific warm pool during boreal summer (Jiang and Waliser 2008; Maloney et al. 2008). Observations and modeling studies indicate a strong link between east Pacific ISV and the Madden–Julian oscillation (MJO; e.g., Madden and Julian 2005) during boreal summer (e.g., Maloney and Hartmann 2000a; Maloney et al. 2008; Jiang et al. 2012; Rydbeck et al. 2013), although recent modeling evidence also suggests that the east Pacific may be able to sustain strong ISV when isolated from the west Pacific warm pool (Rydbeck et al. 2013; Jiang et al. 2013).

Global models have had mixed success at producing realistic boreal summer ISV in the east Pacific (Maloney and Esbensen 2005; Jiang et al. 2012, 2013). Jiang et al. (2013) analyzed 16 models from the Coupled Model Intercomparison Project phase 5 (CMIP5) database and demonstrated that only seven models could produce a realistic spatial pattern of east Pacific ISV, although not all of these seven models produced realistic amplitude. Regional coupled models have demonstrated some success at producing realistic east Pacific ISV, although previous studies have also shown substantial sensitivity of simulation quality to the domain size and realism of the model basic state (Small et al. 2011; Rydbeck et al. 2013). A primary goal of this study is to conduct a process-oriented model diagnostic analysis to help determine reasons for global model success or failure at simulating east Pacific ISV. This effort is inspired by the process-oriented model diagnosis effort of the Working Group on Numerical Experimentation MJO Task Force, which has been developing process-oriented model diagnostics to distinguish reasons for good and poor MJO simulations (Wheeler et al. 2013; Zhang et al. 2013; Kim et al. 2014; Benedict et al. 2014). This effort has gained further impetus as a result of the process-oriented diagnostics effort for North American climate being conducted by the National Oceanic and Atmospheric Administration Modeling, Analysis, Predictions, and Projections Program CMIP5 Task Force.

Previous modeling studies have presented hypotheses on important factors for realistic simulation of boreal summer east Pacific ISV. In observations, latent heat flux anomalies are positive during the enhanced convection phase because southwesterly surface wind anomalies add constructively to the basic-state southwesterly surface flow (Maloney and Esbensen 2007). Jiang et al. (2013) and Rydbeck et al. (2013) suggested that models need to produce realistic climatological low-level winds to produce a realistic simulation of east Pacific ISV to allow positive latent heat flux anomalies to support enhanced intraseasonal convection. Previous model sensitivity tests have demonstrated that removing wind-induced surface flux feedbacks can severely degrade the quality of ISV in both the east Pacific and in the broader tropics (Maloney and Esbensen 2005; Maloney and Sobel 2004; Sobel et al. 2010; Maloney et al. 2010).

Maloney and Esbensen (2005) demonstrated that more realistic east Pacific ISV could be generated in a model by making its convective parameterization more sensitive to free tropospheric moisture. The findings of Jiang et al. (2012) support the importance of enhanced convective moisture sensitivity, in that two models exhibiting the best simulations of east Pacific ISV were also models in which sensitivity of deep convection to free tropospheric moisture was enhanced. One of these models was characterized by increased convective entrainment in a conventional parameterization, and another employed the concept of superparameterization (e.g., Randall et al. 2003) in which two-dimensional cloud-resolving models (CRMs) are embedded in global model grid boxes to explicitly simulate some aspects of convection. This approach heightens the convective moisture sensitivity of the model (e.g., Thayer-Calder and Randall 2009). Jiang et al. (2012) also argued that high horizontal resolution can aid simulation of east Pacific ISV. The impacts of ocean coupling on east Pacific ISV are unclear. Maloney and Kiehl (2002) used uncoupled and coupled versions of a global model to demonstrate that ocean coupling makes the east Pacific ISV stronger and more realistic. However, Small et al. (2011) found little tangible impact of coupling when examining uncoupled and coupled versions of a regional model.

More work has been done for parts of the tropics other than the east Pacific in diagnosing improved simulations of ISV, including the MJO. Several of these diagnostic efforts have been inspired by the theoretical concept that the MJO is a moisture mode (Raymond 2001; Raymond and Fuchs 2009; Maloney et al. 2010; Sobel and Maloney 2013). A moisture mode is a balanced disturbance that exists in a state of weak tropical temperature gradients (WTG; e.g., Charney 1963; Yano and Bonazzola 2009), such that the fundamental dynamics of the mode can be described by the processes controlling the tropospheric moisture field (Sobel et al. 2001;

Raymond et al. 2009). Convection that is strongly tied to column water vapor variations (Bretherton et al. 2004; Sahany et al. 2012) is associated with balanced vertical motion field that influences the large-scale horizontal flow through vertical vorticity generation. In conjunction with condensational and cloud feedback processes, moisture advection and forcing of surface entropy fluxes associated with the vertical and horizontal flow field can modify the moisture distribution (e.g., Pritchard and Bretherton 2014). Inspired by earlier work by Thayer-Calder and Randall (2009), Kim et al. (2014) composited Indo-Pacific warm pool relative humidity as a function of precipitation rate and showed that models with better MJO simulations show a large spread in lower free tropospheric humidity between the highest and lowest percentile precipitation events.

Researchers are also increasingly using the column-integrated moist static energy (MSE) and moist entropy budgets to diagnose the efficacy of tropospheric moistening processes in the context of model ISV (e.g., Maloney 2009; Andersen and Kuang 2012; Maloney and Xie 2013; Cai et al. 2013; Pritchard and Bretherton 2014; Benedict et al. 2014). Under WTG theory, the vertically integrated MSE budget effectively becomes a moisture tendency equation (e.g., Benedict et al. 2014). In addition to examining the importance of MSE sources and sinks for destabilizing and propagating the MJO (e.g., Maloney 2009; Andersen and Kuang 2012), much recent diagnostic analysis has also involved interpreting the horizontal and vertical advection terms in the MSE budget.

In particular, Neelin and Held (1987) developed a term called gross moist stability (GMS), which they defined as the MSE export from the column by vertical advection per unit vertical mass flux. What this measure of GMS effectively represents under conditions of WTG is the efficiency with which convection and associated divergent circulations discharge moisture from the column per unit convective activity. The numerator of GMS represents the cancellation of vertical moisture advection and dry static energy export by the vertical mass flux (neglecting radiation, approximately equal to condensational drying in WTG theory). Raymond and Fuchs (2009) and Raymond et al. (2009) generalize GMS to also include the effects of horizontal advection, and argue that the vertical component of GMS should be negative (or effectively negative) to support the moisture anomalies that maintain a moisture mode. They also argued that GMS can be positive, as long as MSE sources such as surface fluxes and radiative feedbacks are large enough to overcome MSE discharge by convection and associated divergent circulations. Hannah and Maloney (2011) demonstrated in a GCM that increasing the moisture sensitivity of the model convective scheme produces negative time-mean GMS and stronger ISV. Benedict et al. (2014) looked at three model pairs, one each with a simulation having a poor MJO and a perturbed model with improved MJO. GMS was systematically lower for the models with improved MJO simulations, indicating that it is easier to maintain intraseasonal moisture anomalies and hence convective anomalies. Pritchard and Bretherton (2014) showed that GMS systematically lowered in a series of simulations of the superparameterized Community Atmosphere Model (SP-CAM) as the treatment of horizontal moisture advection was modified and ISV increased in the process.

In this paper we diagnose eight global atmospheric simulations that demonstrate differing abilities to simulate east Pacific warm pool ISV during boreal summer. Inspired by the efforts discussed above, we will attempt to determine suitable diagnostics that can distinguish why some models produce better simulations of east Pacific ISV than others. We cannot be entirely comprehensive here, and so our analysis will involve diagnostics inspired by the moisture mode paradigm for tropical ISV, in which the processes that regulate the tropospheric moisture field describe the essential dynamics. The importance of such theory to east Pacific ISV has been suggested by previous modeling studies including those by Maloney and Esbensen (2005) and Jiang et al. (2012, 2013). Section 2 describes the global models employed in this study and the observational fields used for comparison. Section 3 introduces the complex empirical orthogonal technique used to assess model fidelity in reproducing the leading east Pacific intraseasonal mode. Section 4 provides examples of some diagnostics that are not strongly related to model success. Section 5 describes diagnostics based on relative humidity composites and the moist entropy budget that have the capability to distinguish good and bad simulations of east Pacific ISV. Section 6 provides a discussion and conclusions.

2. Description of models and observations

We employ the same suite of models used by Benedict et al. (2014) in a process-oriented diagnostics study to demonstrate that the moist entropy budget can explain MJO simulation success or failure. A subset of these models were also used in Benedict et al. (2013), which documented how modifying the convection scheme in the Geophysical Fluid Dynamics Laboratory (GFDL) Atmosphere Model version 3 (AM3) affected the simulation of ISV. Although Benedict et al. (2013, 2014) describe these models in some detail, we will briefly summarize

TABLE 1. Summary of the models used in this study. The numbers of model levels are designated with a prefix L, the ZM95 stands for the Zhang–McFarlane (Zhang and McFarlane 1995) scheme, and the Tokioka et al. (1988) minimum entrainment threshold is represented by α. See text for further details.

		Deep convection parameterization			
Model	GCM resolution	Scheme	Closure	Trigger	Downdrafts?
AM2-CTL	2° lat × 2.5° lon, L24	RAS	CAPE relaxation	$\alpha = 0.025$	No
AM2-TOK	2° lat × 2.5° lon, L24	RAS	CAPE relaxation	$\alpha = 0.1$	No
AM3-CTL	~(163–231) km, L32	Donner	CAPE relaxation	—	No
AM3-A	~(163–231) km, L32	Donner	Zhang (2002) (CAPE based)	Time-integrated low-level parcel lifting	No
AM3-B	~(163–231) km, L32	Donner	Zhang (2002) (CAPE based)	Time-integrated low-level parcel lifting	Yes
AM3-C	~(163–231) km, L32	Donner	Zhang (2002) (CAPE based), entrainment dilution	Time-integrated low-level parcel lifting	Yes
CAM3.0	T42 [~(2.8° × 2.8°)], L30	ZM95	CAPE consumed at specified rate	—	Yes
SP-CAM-AMIP	T42 [~(2.8° × 2.8°)], L30	Explicit (4-km CRM)	—	—	Explicit

them here. Table 1 also provides salient features of these simulations, including information on resolution and physical formulation of the models. We employ two versions of the GFDL Atmosphere Model version 2 (AM2). The first AM2 version, which we refer to as AM2-CTL, is the standard version of the AM2 (Anderson et al. 2004) that uses a relaxed Arakawa–Schubert (RAS) convection scheme to parameterize deep atmospheric convection. The second AM2 version, which we call AM2-TOK, is identical to AM2-CTL, but implements a strong minimum entrainment threshold in the RAS scheme that makes convection more sensitive to free tropospheric humidity (Tokioka et al. 1988). Other studies have also demonstrated that inclusion of such a minimum entrainment threshold improves the simulation of tropical ISV (e.g., Tokioka et al. 1988; Kim et al. 2011b; Hannah and Maloney 2011).

We use four versions of the GFDL AM3 (Donner et al. 2011). As described in Donner et al. (2011), the deep convection scheme in AM3 includes components for deep convection and mesoscale anvils, the latter of which are important in simulating cloud–radiative interactions. The control version of AM3 used here (which we refer to as AM3-CTL) has a convective closure based on convective available potential energy (CAPE), and convection is suppressed if convective inhibition (CIN) rises above 100 J kg^{-1}, or CAPE falls below 1000 J kg^{-1}. We also employ three modified versions of AM3. In AM3-A, the Zhang (2002) closure is used for deep convection, in which CAPE generation due to temperature fluctuations in the free troposphere are balanced by CAPE consumption due to cumulus convective activity. In addition, AM3-A adds a lower tropospheric convective trigger based on the time-integrated vertical velocity. AM3-B is identical to AM3-A, except that more convective condensate is exposed to the large-scale environment and allowed to evaporate, rather than going into mesoscale anvils, and a fraction of convective condensate can also generate downdrafts. We note that the simulation we refer to as AM3-B was the modified AM3 simulation employed in Benedict et al. (2014). AM3-C makes the further modification that all CAPE calculations include entrainment dilution, with the assumption of a constant fractional entrainment rate of 0.2 km^{-1}. Benedict et al. (2013) showed that the modified versions of AM3 produce superior ISV to that in AM3-CTL.

We also analyze two versions of the National Center for Atmospheric Research (NCAR) Community Atmosphere Model version 3 (CAM; Collins et al. 2006). The standard version of CAM uses a deep convective parameterization based on the mass flux scheme of Zhang and McFarlane (1995), which is closed on CAPE and has a parameterization of convective downdrafts. SP-CAM (Khairoutdinov et al. 2008; Benedict and Randall 2009) replaces the conventional parameterizations of CAM with a two-dimensional cloud system–resolving model within each host model grid box. The 2D high-resolution models are oriented north–south, composed of 32 horizontal grid boxes, and have a horizontal grid resolution of 4 km. The superior performance of SP-CAM at simulating tropical ISV has been well documented by previous studies (e.g., Benedict and Randall 2009; Thayer-Calder and Randall 2009; Zhu et al. 2009).

As described in Benedict et al. (2014), AM2 and AM3 simulations are integrated for 10 years using a climatological mean seasonal cycle SST boundary condition derived from 1981 to 2000. We also use 10 years of CAM and SP-CAM simulations integrated using an observed SST boundary condition during

1987–96. These years are a subset of longer CAM and SP-CAM simulations that were conducted over 1985–2004, although we do not find that our diagnostic analysis presented below significantly differs if we use a different 10-yr subset of these longer simulations, or if the entire record is used.

We also conduct a diagnostic analysis of satellite-derived precipitation and reanalysis fields. The Tropical Rainfall Measuring Mission (TRMM) 3B42 rainfall product (Huffman et al. 2007) is used to assess observed east Pacific intraseasonal precipitation variability, and the Interim European Centre for Medium Range Weather Forecasts (ECMWF) Re-Analysis (ERA-I) product is employed to assess observed dynamic and thermodynamic variables (Dee et al. 2011). While we refer to ERA-I fields as ''observations'' within this study, it should be noted that reanalysis products often have substantial analysis increments introduced in the process of data assimilation that are partially due to deficiencies in reanalysis model physics (e.g., Mapes and Bacmeister 2012). These contribute to the residual in reanalysis moisture and energy budgets (e.g., Back and Bretherton 2006; Landu and Maloney 2011a). Both observational datasets were used during 1999–2008, a 10-yr period during which both the satellite precipitation dataset and reanalysis were available. Before the diagnostics below are computed, all model and observed fields were daily averaged and linearly interpolated to a common 2.5° by 2.5° horizontal grid.

3. Assessment of ISV using complex EOF analysis

As in previous studies (Maloney et al. 2008; Small et al. 2011; Jiang et al. 2013), we use complex empirical orthogonal function (CEOF) analysis on 30–90-day bandpass-filtered precipitation fields during June to October to document the leading modes of east Pacific ISV in models and observations. CEOF analysis is like EOF analysis, except that the data matrix used in the eigenfunction analysis is complex, constructed using the original data matrix plus i times the quadrature function of the original data matrix (Barnett 1983; Horel 1984). The quadrature function is computed using a Hilbert transform over the entire data record, before subsetting the entire complex matrix to select only boreal summer months for input into the eigenvector calculation. Maloney et al. (2008) provide more detail on the CEOF technique applied here.

Figure 1 shows the spatial amplitude of the leading CEOF computed in the region shown for the TRMM observations and the eight models. The amplitude time series are normalized, such that the amplitudes (mm day^{-1}) shown in Fig. 1 provide a direct comparison of the strength of the leading mode of ISV among the models and observations. The total percent variance explained for observations and each model is listed above each panel. Figure 2 shows the corresponding plot of spatial phase for the leading mode, shown only where the local variance explained exceeds 5%, and also focused over a more limited region of the warm pool than Fig. 1. Increasing spatial phase indicates the direction of phase propagation as time increases.

Figure 1 shows that the models have differing abilities to capture the magnitude and spatial distribution of amplitude for the leading CEOF mode. For example, AM2 demonstrates too weak amplitude, with the variance maximum concentrated near the coast. AM2-TOK has significantly stronger amplitude, but has a variance maximum over southern Mexico. Models such as AM3-A and SP-CAM demonstrate an improved spatial distribution and magnitude of the leading mode amplitude, although they also exhibit some significant differences relative to observations. To more precisely quantify the east Pacific warm pool amplitude of the leading mode in the models relative to observations, the average amplitude was calculated over a box spanning 5°–20°N, 90°–120°W, which encompasses the region of strongest observed variance. The y axis of Fig. 3 measures the average amplitude of the leading mode in this region, normalized such that the observed amplitude equals one. It is demonstrated that the perturbed models all have higher amplitude of the leading mode than the control models, with SP-CAM and AM2-TOK having the amplitude closest to observations. A coupled version of the SP-CAM (designated SP-CCSM) is also shown on the plot with similar amplitude to SP-CAM, a simulation that will be discussed in more detail below. It is interesting that this run shows no amplitude difference from SP-CAM, a result consistent with that of Small et al. (2011) that suggested minimal impact from ocean coupling on intraseasonal convective variability in the east Pacific. The perturbed AM3 models exhibit stronger amplitude of the leading mode than TRMM observations. In general, the models exhibit a substantial spread of amplitudes, which will aid our process-oriented diagnosis below.

Figure 2 demonstrates that even models producing reasonable amplitude may not necessarily reproduce the details of observed phase propagation. As in previous studies (e.g., Jiang and Waliser 2008; Maloney et al. 2008), TRMM precipitation fields indicate propagation of 30–90-day precipitation anomalies to the northeast. While some models such as AM3-A and AM2-TOK can produce this pattern of phase propagation with reasonable fidelity, other models such as AM3-B have more

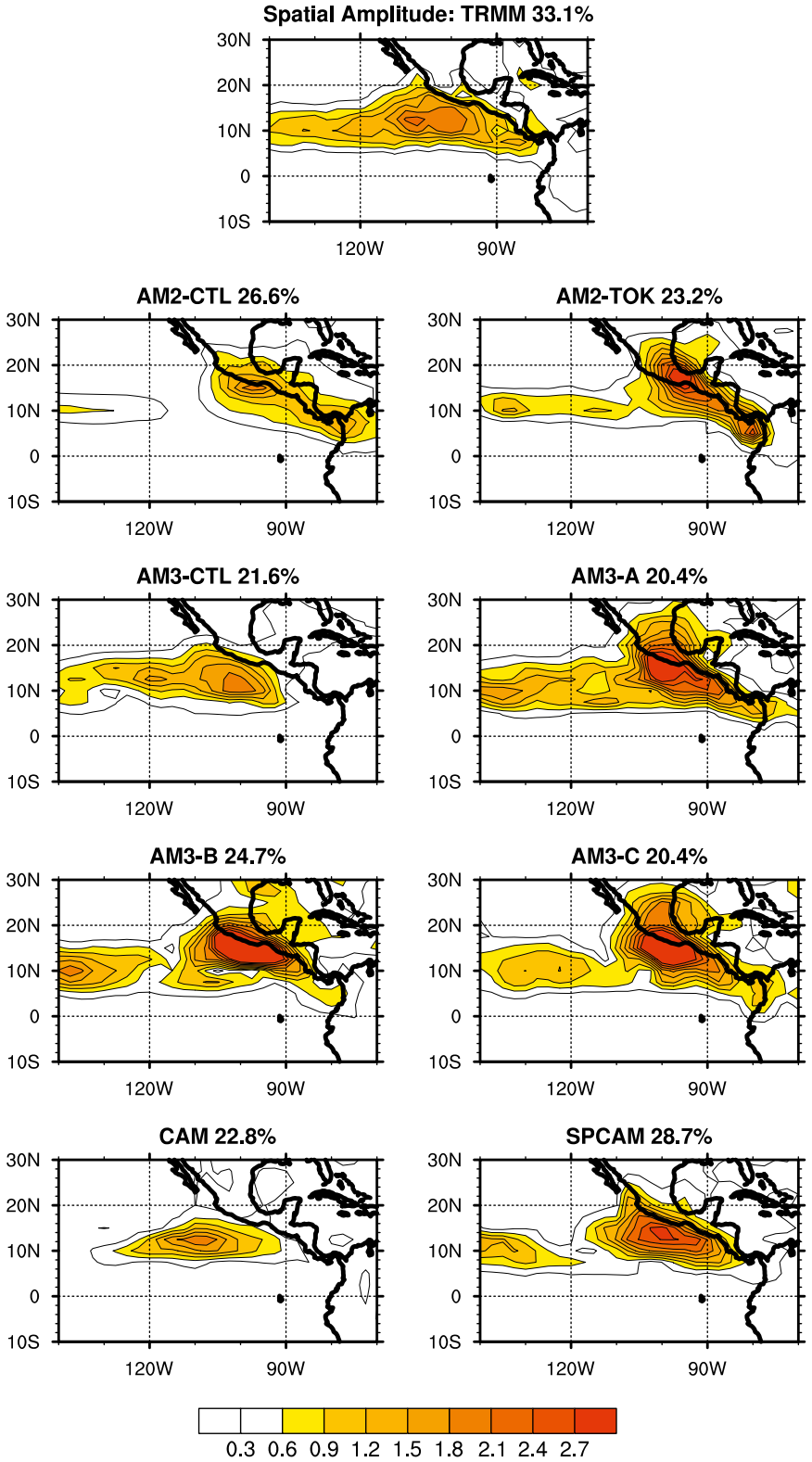

FIG. 1. Spatial amplitude for the leading CEOF mode of the 30–90-day bandpass-filtered precipitation for (top) the TRMM observations and (below) the eight models (mm day^{-1}). The total variance explained by the leading mode is indicated above each panel.

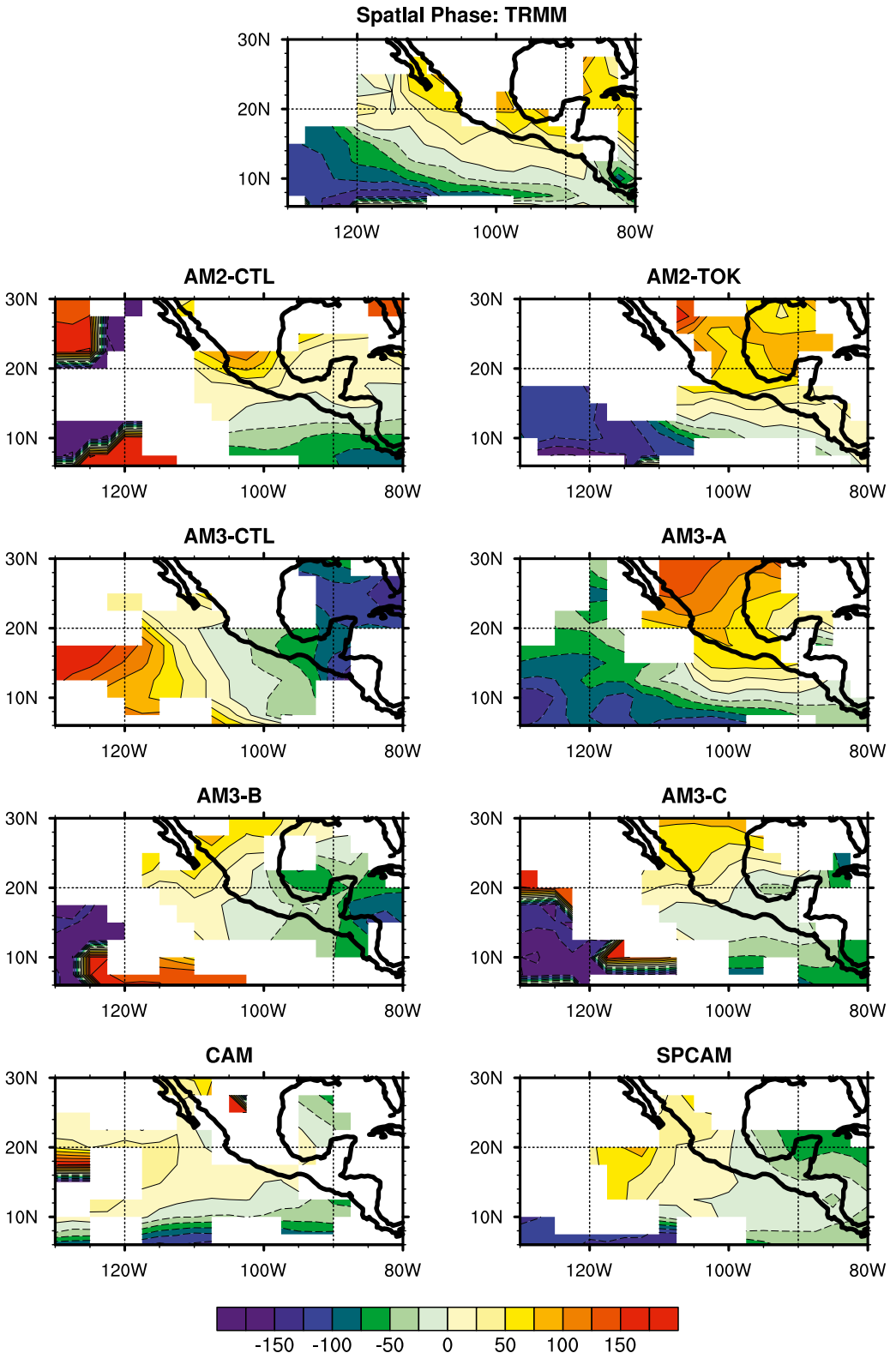

FIG. 2. As in Fig. 1, but for the phase (°). Spatial phase is only plotted where the local explained variance by the leading mode > 5%.

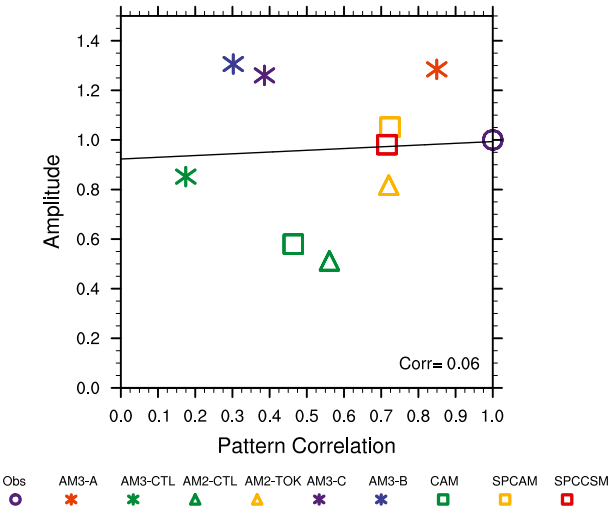

FIG. 3. Amplitude of the leading CEOF mode vs the pattern correlation of the individual spatial propagation patterns with the observed pattern. Amplitude is averaged over the domain 5°–20°N, 120°–90°W and then normalized by the TRMM amplitude. The pattern correlation is conducted over the area 5°–25°N, 140°–80°W. Further details on the pattern correlation calculation are described in the text. The correlation between amplitude and propagation metrics is indicated in the lower right and the least squares regression line is also shown.

difficulty. Several models exhibit a westward component to propagation. To quantify model success at reproducing the pattern of propagation, we follow a procedure similar to that in Jiang et al. (2013). In both models and observations, we multiply the spatial amplitude (Fig. 1) separately by the sine and cosine of spatial phase at each grid point (Fig. 2) to get two spatial maps. Then, the pattern correlations of the two model maps with comparable ones from TRMM observations are computed over the region 5°–25°N, 80°–140°W. The two correlation coefficients derived from comparison of a particular model with TRMM are then averaged. The averaging domain is slightly larger than the amplitude-averaging box used to construct the *y* axis in Fig. 3. We use a larger region for the pattern correlation to better capture some of the nuances of the propagation such as the phase shift across 120°W, but results are not sensitive to modest variations in the averaging domain. While perturbed models generally exhibit improved propagation characteristics relative to their respective control simulations as amplitude increases (Fig. 3), no overall significant correlation exists between leading mode amplitude and skill at capturing propagation. This result is consistent with Jiang et al. (2013). Statistical significance was determined here and in the analyses below by using the *t* statistic at the 95% confidence level assessed against a null hypothesis of zero correlation.

Our pattern correlation analysis in Fig. 3 does amplitude weighting to emphasize regions where precipitation variability is strong. However, repeating the analysis of Fig. 3 without amplitude weighting before constructing the pattern correlations produces a similar insignificant correlation (+0.12) as in Fig. 3, suggesting robustness of our result to variations in the analysis technique. In the sensitivity test without amplitude weighting, AM2-TOK and AM3_A are the models with the best pattern correlation, consistent with visual inspection of Fig. 2.

4. Initial exploration on diagnostics for amplitude and propagation

We now begin our discussion of diagnostics that have been suggested by previous modeling and theoretical studies to have a strong relationship with east Pacific ISV. The initial diagnostics we present in this section will be found to be not significantly related to variations in intraseasonal performance. More successful diagnostics will be presented in section 5. Diagnostics on amplitude will be discussed first, and then more briefly diagnostics related to propagation.

a. Amplitude diagnostics

Previous modeling studies of the east Pacific have suggested a role for wind-induced surface fluxes in destabilizing east Pacific ISV (Maloney and Esbensen 2005; Small et al. 2011; Rydbeck et al. 2013; Jiang et al. 2013), similar to the importance of wind-induced fluxes in destabilizing tropical ISV in other parts of the tropics (e.g., Maloney and Sobel 2004; Sobel et al. 2010). In the east Pacific, it has been thought that climatological surface westerlies aid the generation of strong positive latent heat flux anomalies that support convection, since periods of enhanced convection are associated with surface westerly zonal wind anomalies that add constructively to the mean flow (e.g., Maloney and Esbensen 2005, 2007). Rydbeck et al. (2013) attributed the inability of a regional coupled model to simulate a local intraseasonal mode of variability in the east Pacific to the fact that mean surface winds in the model had a strong easterly bias. Jiang et al. (2013) demonstrated that models producing weaker westerly mean winds in the east Pacific warm pool produced weaker ISV, with amplitude defined using a similar metric as in Fig. 3. We replicate the analysis of Jiang et al. (2013) here, using our eight models.

Figure 4 shows an analysis of area-averaged amplitude versus oceanic surface zonal wind averaged over 5°–20°N, 90°–120°W. Unlike in Jiang et al. (2013), this set of models exhibits an insignificant negative correlation between mean surface zonal wind and amplitude of the

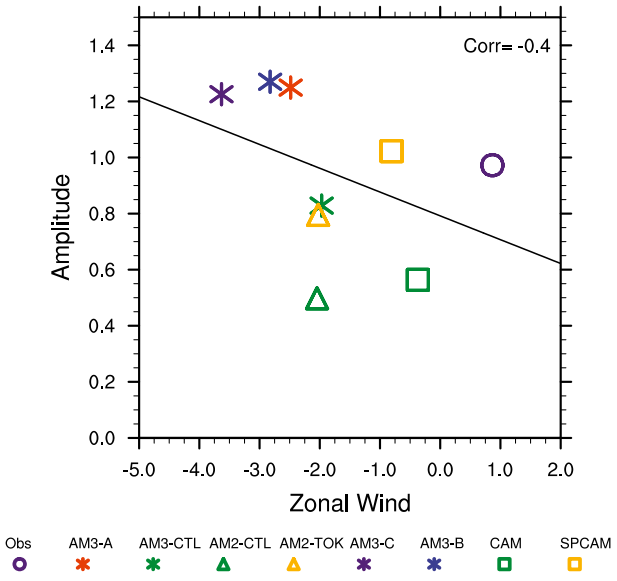

FIG. 4. As in Fig. 3, but vs the June–October average ocean surface zonal wind. The correlation is shown in the upper right.

leading CEOF mode. While mean zonal winds in ERA-I are slightly westerly in the area average, all of the models exhibit mean easterly winds. This suggests that stronger wind-induced flux feedbacks, at least those driven by zonal wind anomalies, are not necessary to support strong ISV in this set of models. To further support this point, 30–90-day latent heat flux anomalies are regressed onto a 30–90-day precipitation time series averaged in a 10° × 10° box centered at 11°N, 101°E, near the center of the observed amplitude maximum of the leading mode shown in Fig. 1. Figure 5 indicates that the strength of the regression coefficient [$W\,m^{-2}\,(mm\,day^{-1})^{-1}$] is generally weaker in the models than observations (ERA-I reanalysis), consistent with a weaker wind–evaporation feedback and tendency for models to have an easterly basic state. In all models, surface wind speed is enhanced in regions of enhanced surface flux when conducting a similar regression analysis (not shown here), although the wind speed regression coefficients are weaker than observed with the exception of CAM. While CAM exhibits the strongest feedback of the models, consistent with a more realistic mean state, this model has the second lowest amplitude. In general, these results suggest that a strong wind–evaporation feedback is not sufficient to produce realistic ISV in a model, although previous studies have suggested that its absence can have deleterious effects on a model's east Pacific ISV (e.g., Maloney and Esbensen 2005; Rydbeck et al. 2013).

An interesting question is why the wind–evaporation feedback in all models in Fig. 5 is positive even though the mean winds at 850 hPa are easterly. It turns out that in most models the enhanced wind speed is dominated by the meridional wind anomalies. This was determined by reconstructing the surface wind speed from daily u and v components, but before the speed was calculated and anomalies derived, either the u or v components were low-pass filtered to remove intraseasonal variability. Simply retaining intraseasonal variability in the v component reproduces the majority of the wind speed anomalies in most models. The mean surface meridional flow in the warm pool is southerly in all models, and the anomalous southerly meridional flow during convective events adds constructively to the mean winds. Only in ERA-I and AM2-CTL do intraseasonal zonal wind anomalies dominate the wind speed anomaly.

Kim et al. (2014) composited the vertical profile of relative humidity as a function of precipitation rate, following the work of Thayer-Calder and Randall (2009), and then examined average relative humidity in the lower free troposphere. Kim et al. (2014) found that the difference in relative humidity between upper and lower percentiles of model precipitation events was a good measure of MJO performance, consistent with the tendency for models producing stronger convective moisture sensitivity to produce a stronger MJO.

Before using a method similar to that of Kim et al. (2014), we first examine the amplitude of the leading east Pacific intraseasonal mode versus 500–850-hPa mass-weighted relative humidity for the top 1% of daily averaged rain events. This was previously considered as a metric to assess MJO performance in the Kim et al. (2014) study, before being dropped in favor of the metric based on the relative humidity difference between upper and lower percentiles (D. Kim 2014, personal communication). We conduct such compositing using daily average precipitation and relative humidity on a point-by-point basis in the region spanning 5°–20°N, 90°–120°W during June–October. ERA-I relative humidity was used as observations. Figure 6 shows an insignificant negative correlation of −0.29 between relative humidity in the top 1% of precipitation events and amplitude of the leading mode. Hence, this diagnostic is not successful at discriminating amplitude of the leading mode of east Pacific ISV. Results are similar if the top 5% or top 10% of precipitation events is used. However, we will show in section 5 below that a metric based on the relative humidity difference between the highest and lowest precipitation events such as used in Kim et al. (2014) is able to discriminate between models of strong and weak ISV.

b. *Propagation*

Jiang and Waliser (2008) argued that easterly shear of the zonal flow in the east Pacific during boreal summer

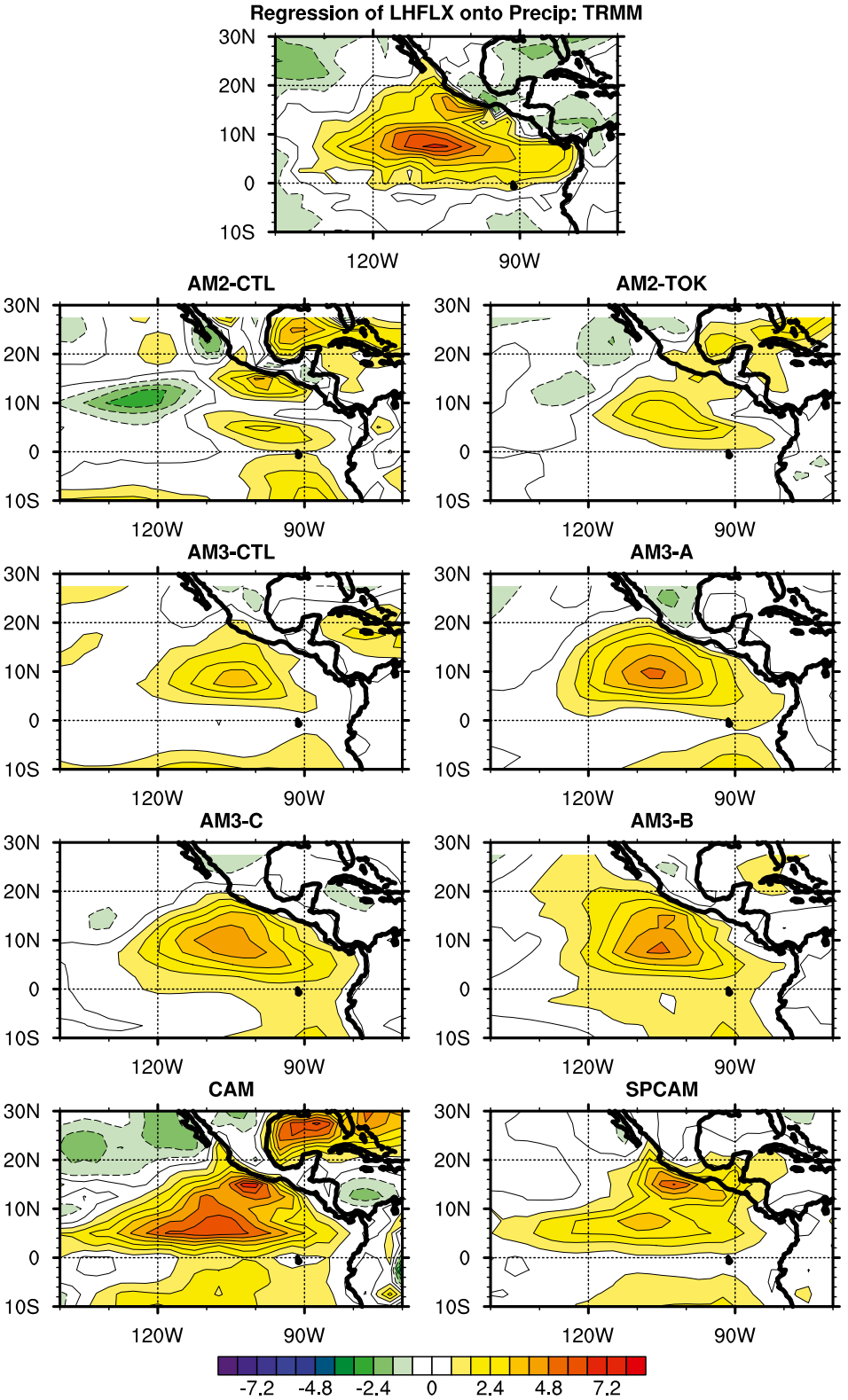

FIG. 5. As in Fig. 1, but for the regression [W m^{-2} (mm day^{-1})$^{-1}$] of 30–90-day bandpass-filtered latent heat flux anomalies onto a 30–90-day precipitation time series averaged in a 10° × 10° box centered at 11°N, 101°E. Data during June–October are used.

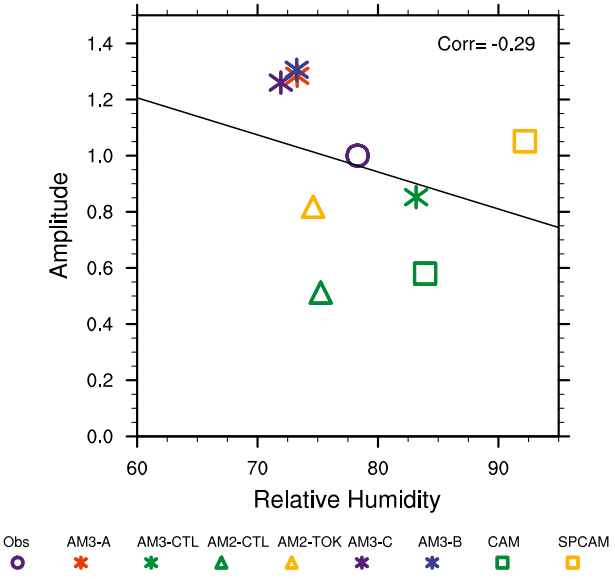

FIG. 6. As in Fig. 3, but vs the June–October average 500–850-hPa mass-weighted relative humidity for the top 1% of daily average precipitation events. Relative humidity and precipitation are considered on a point-by-point basis in the domain. The correlation is shown in the upper right.

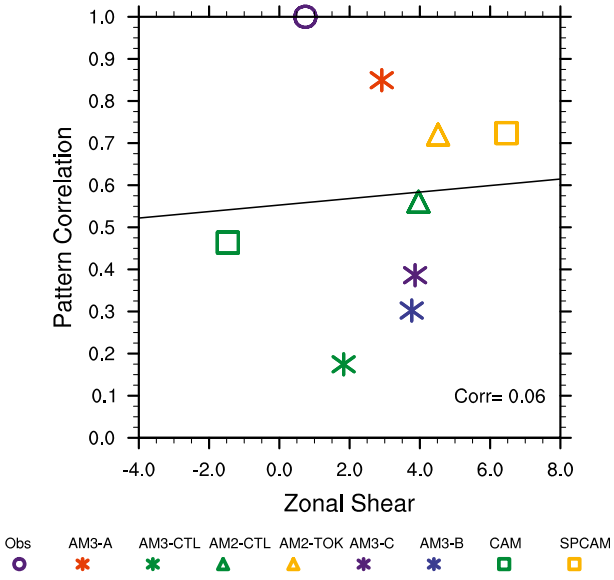

FIG. 7. Pattern correlation of the individual spatial propagation patterns with the observed pattern as defined in Fig. 3 vs the June–October mean zonal wind shear (200- − 850-hPa zonal wind) averaged over the domain 5°–25°N, 140°–80°W. The correlation is shown at the bottom right and the least squares regression line is also shown.

could aid northward propagation of intraseasonal precipitation and wind anomalies. The mechanism relies on positive vorticity generation to the north of existing positive precipitation regions through anomalous vertical velocity acting on the environmental zonal easterly wind shear. To test whether models with stronger easterly shear produce a more realistic pattern of propagation, we compare average June–October zonal shear (defined as the difference between 200-hPa and 850-hPa zonal wind) in the region spanning 5°–25°N, 80°–140°W to the correlation of the spatial propagation pattern with observations, as defined in Fig. 3. Figure 7 shows little relationship between zonal shear and the quality of the propagation pattern, indicating that mean zonal shear is not a good predictor of success at producing the observed propagation pattern. Similar results are obtained if we focus only on the region of strongest observed amplitude (5°–20°N, 90°–120°W), where the wind shear is more easterly in all cases (not shown). When considering only northward propagation, comparison of Figs. 2 and 7 indicates little relationship between the tendency to produce northward propagation and the strength of easterly shear. We also tested whether easterly mean state biases at 850 hPa could contribute to the tendency of many models to produce more prominent westerly propagation than observed (Fig. 2). The hypothesis is that stronger mean easterlies would foster westward moisture advection and hence favor westward propagation (e.g., Maloney et al. 2010). No significant correlation exists between the quality of the propagation pattern and strength of easterly flow in the warm pool (not shown here), casting doubt on this hypothesis.

SP-CAM is an interesting case of a model that has realistic amplitude but substantial deficiencies in propagation characteristics (Figs. 2 and 3). SP-CAM is dominated by westward propagation as diagnosed by the leading intraseasonal mode, a fact confirmed by a lag-regression analysis of precipitation onto itself (not shown). Previous studies on ISV of the Indian monsoon system have argued that ocean coupling may improve propagation characteristics of Indian Ocean boreal summer ISV in models, in particular aiding northward propagation (e.g., Fu and Wang 2004; Wang et al. 2009; Klingaman et al. 2008; Sharmila et al. 2013), while other studies have suggested only modest impacts from coupling on propagation (e.g., Bellon et al. 2008). Of particular relevance to this study is the work of DeMott et al. (2011), who showed that coupling the SP-CAM to an interactive ocean improved northward propagation of the boreal summer intraseasonal oscillation in the Indian Ocean.

To test whether ocean coupling improves the propagation characteristics of SP-CAM, we examine a 10-yr simulation of the superparameterized NCAR Community Climate System Model (hereafter referred to as SP-CCSM), in which the SP-CAM is coupled to the Community Climate System Model (CCSM) ocean model

(Collins et al. 2006). SP-CCSM model details are described in Stan et al. (2010). Figure 3 indicates that ocean coupling does not substantially change the pattern correlation of the spatial propagation pattern relative to observations. The spatial phase corresponding to the leading mode of the SP-CCSM simulation looks nearly identical to that of SP-CAM in Fig. 3 (not shown here). The lack of changes in propagation characteristics and amplitude of the leading mode in Fig. 3 between coupled and uncoupled versions of SP-CAM suggest that coupling has minimal impact on 30–90-day time scale precipitation variability in the east Pacific, consistent with the results of Small et al. (2011).

5. Effective diagnostics for amplitude

a. Relative humidity composites on precipitation

As mentioned in section 4 above, Kim et al. (2014) introduced a moisture sensitivity diagnostic as in Fig. 6, but rather than using the relative humidity for the top 1% of precipitation events, the difference in lower free tropospheric humidity between the top and bottom percentiles of precipitation events was assessed against model MJO performance. This diagnostic produced a significant relationship with MJO performance in the Kim et al. (2014) study. A greater spread in relative humidity between the top tier and bottom tier of precipitation events is consistent with a model having greater convective sensitivity to environmental moisture, although it can also arise from stronger MJO events producing stronger moisture anomalies.

To test such a diagnostic, we repeat our analysis of Fig. 6 except that we use the difference between the top 5% and bottom 10% of precipitation events and 500–850-hPa mass weighted average relative humidity. Figure 8 indicates that a significant correlation of 0.71 exists between the amplitude of the leading mode and this relative humidity difference. This is a comparable correlation to that derived from Kim et al. (2014) assessing a related metric against MJO performance. This analysis would suggest that models with greater moisture sensitivity of convection tend to produce stronger east Pacific ISV. Interestingly, this result is not necessarily robust within a model, as little relative humidity difference exists between highest and lowest precipitation events for different versions of the GFDL AM3. Comparison of Figs. 6 and 8 also suggests that while increased moisture sensitivity of a model may be important for producing strong ISV in the east Pacific, no common relative humidity threshold for when the most intense rainfall events occur exists among models having similar amplitude.

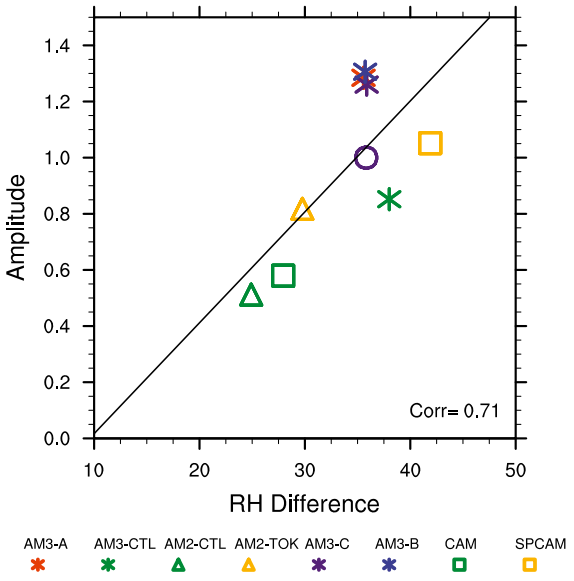

FIG. 8. As in Fig. 6, but between the top 5% and bottom 10% of daily average precipitation events. The correlation is shown at the bottom right.

b. Gross moist stability

GMS provides a measure of moist entropy or MSE export per unit convective activity (Neelin and Held 1987; Raymond et al. 2009). Benedict et al. (2014) demonstrated using three model pairs each having a strong and weak MJO that models with stronger simulations of the MJO are characterized by lower time-mean GMS, behavior dictated by the vertical component of GMS. This finding is consistent with moisture mode theory in that models with lower GMS are more likely to sustain the moisture anomalies that support MJO convection. We define GMS in an identical manner to Benedict et al. (2014) such that the vertical component of GMS (VGMS) can be represented as follows:

$$\mathrm{VGMS} = -\frac{T_R\left\langle \omega \frac{\partial s}{\partial p} \right\rangle}{L\langle \nabla \cdot (r\mathbf{V}) \rangle}, \tag{1}$$

where s is the moist entropy as defined in Benedict et al. (2014), r is the water vapor mixing ratio, $T_R = 273.15$, L is the latent heat of vaporization, ω is the pressure velocity, $\mathbf{V}$ is the horizontal wind vector, and the horizontal gradient operator is taken on a pressure surface. Angled brackets represent a mass-weighted integral from the surface to the tropopause, here taken to be 100 hPa. Moisture convergence is used here as a measure of convective intensity, consistent with Raymond et al. (2009).

Similarly, the horizontal component is GMS (HGMS) is defined as

$$\mathrm{HGMS} = -\frac{T_R\langle \mathbf{V}\cdot\nabla s\rangle}{L\langle \mathbf{V}\cdot(r\mathbf{V})\rangle} \qquad (2)$$

and the total GMS (TGMS) is represented as the sum of (1) and (2).

As described in Benedict et al. (2014), before computing the quotients in (1) and (2), the numerator and denominator are smoothed with a 7.5° by 7.5° sliding box spatial smoother, and land points are omitted from the calculation. Further, to avoid division by zero, times when the denominator has absolute value less than 5 W m^{-2} are omitted from the time averages described below. Further details on the computation of GMS are contained in Benedict et al. (2014). In the analysis presented here, we take a multiyear June–October average of VGMS, HGMS, and TGMS for the east Pacific in the region 5°–20°N, 90°–120°W for consistency with the amplitude averaging region discussed above.

Figure 9 shows scatterplots of the leading mode amplitude versus a) VGMS, b) HGMS, and c) TGMS. The amplitude of the leading mode has a large and significant correlation of −0.9 with VGMS, a result consistent with the MJO results of Raymond and Fuchs (2009), Hannah and Maloney (2011), and Benedict et al. (2014). VGMS approaches −0.2 for the models with strongest variability, and 0.1 for the model (AM2) with weakest variability. SP-CAM is most consistent with ERA-I in amplitude and VGMS, having a VGMS of about −0.08. This result supports the contention that lower VGMS helps to maintain moisture anomalies that support intraseasonal convection (e.g., Raymond and Fuchs 2009). HGMS (Fig. 9b) exhibits a significant positive correlation of 0.8 with the leading mode amplitude, and comparison of Figs. 9a and 9b suggests a certain degree of compensation between VGMS and HGMS in models such that when one gets larger, the other smaller. It is not surprising that this would happen if column moist entropy sources and sinks remain approximately unchanged, and advective transports are required to maintain energy balance. Another possible interpretation of Figs. 9a and 9b is that if more negative VGMS helps to destabilize intraseasonal disturbances and maintain strong convection and moisture anomalies, more organized horizontal rotational flows result that increase the horizontal advective export per unit convective activity. Stronger synoptic eddy activity accompanying stronger intraseasonal disturbances might contribute to enhanced horizontal advection, as suggested by the results of Maloney (2009) and Andersen and Kuang (2012). A related difference in observed moist entropy budget

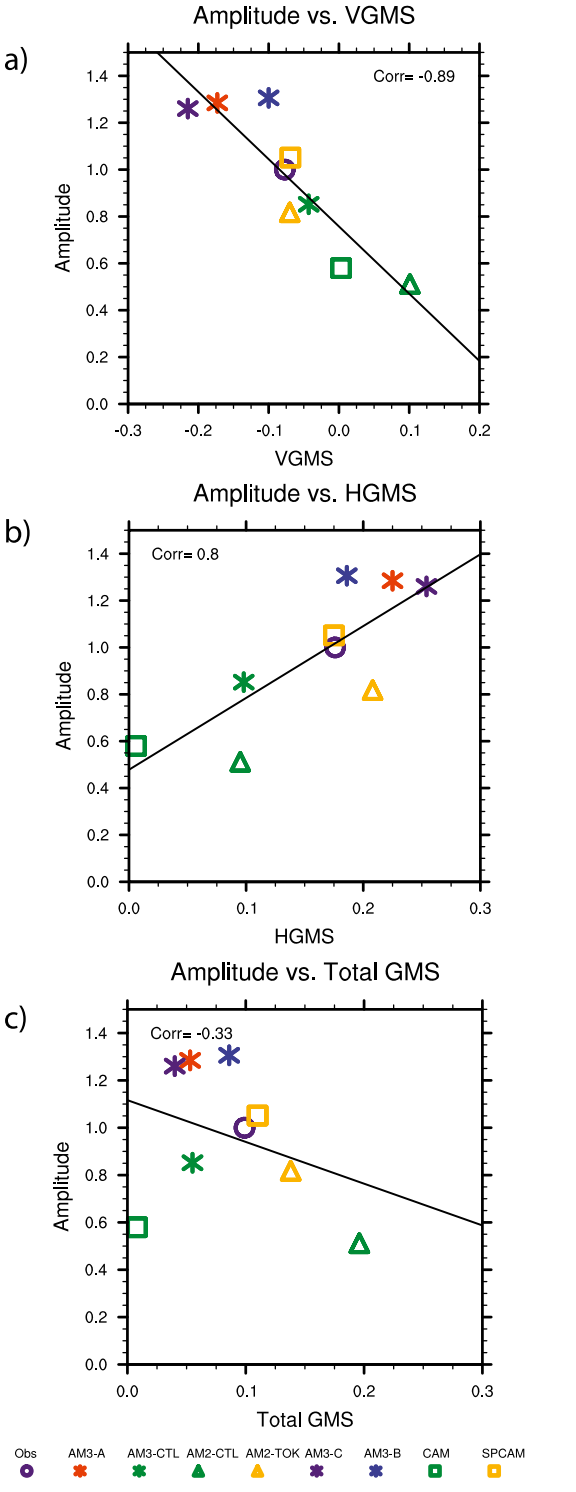

FIG. 9. Amplitude of the leading CEOF mode vs the June–October average GMS: (a) vertical component, (b) horizontal component, and (c) total. Amplitude is averaged over the domain 5°–20°N, 120°–90°W; and GMS is averaged over oceanic points in the same domain. Amplitude is normalized by the TRMM amplitude. The correlation is shown at the upper right and the least squares regression line is also shown.

advective terms is seen between the Indo-Pacific warm pool and the east Pacific ITCZ. The east Pacific ITCZ is characterized by negative VGMS and enhanced horizontal advective drying and cooling (with a strong contribution from synoptic eddies), while in the Indo-Pacific warm pool VGMS is higher and horizontal advection per unit convective activity more muted (e.g., Back and Bretherton 2006; Peters et al. 2008).

Figure 9c demonstrates no significant relationship between TGMS and amplitude, unlike the relationship shown in Benedict et al. (2014) for the MJO. The correlation between amplitude and TGMS in Fig. 9c is −0.3. This result is consistent with the compensation between VGMS and HGMS seen in Figs. 9a and 9b, and suggests that it is low VGMS that is important for strong ISV, as suggested by Raymond and Fuchs (2009).

To further support the relationship between VGMS and amplitude, we subsetted the observed record into 10 individual years, and computed the correlation and regression coefficient of mean June–October GMS versus leading mode amplitude for individual years. A correlation of −0.5 was produced, although this value was just below the 95% significance threshold. The regression coefficient is $-3.8\,\mathrm{mm\,day^{-1}}$, broadly comparable to the $-2.9\,\mathrm{mm\,day^{-1}}$ value of Fig. 9a. This result is somewhat encouraging, especially as one would not expect an intraseasonal event to always occur even if VGMS were low, since sufficient triggering might not always be available or destructive interference from the west Pacific may be present (e.g., Rydbeck et al. 2013).

To provide some insight into the causes of variations in VGMS among models, we examine vertical profiles of mean June–October normalized pressure velocity ω and MSE averaged for oceanic points in the region 5°–20°N, 90°–120°W. The MSE profiles very closely resemble moist entropy profiles. We note that the mean profiles appear suitable for providing insight into the differences in VGMS among the models, because profiles during periods of enhanced and suppressed convection appear to simply minimize or exaggerate differences among models seen in the mean profiles, while not being qualitatively different in vertical structure. Figure 10 shows mean June–October MSE and ω profiles for the control and perturbed version of AM2, AM3, and CAM–SP-CAM. Omega is normalized in all plots such that the mass-weighted vertical integral is equal to one for all model profiles. The process of normalization has reversed the sign of ω in Fig. 10 relative to the actual value for these mean convecting regions.

In all comparisons the perturbed models with stronger variability have a more top-heavy mean ω profile in the east Pacific. This tendency is most pronounced for AM2 and CAM–SP-CAM (Figs. 10a,e), and more subtle, but still present for AM3 (Fig. 10c). Peters and Bretherton (2006) describe how a more top-heavy omega profile would tend to increase VGMS in the presence of a common MSE profile, since MSE export in the upper troposphere is increased. Hence, the changes in mean vertical velocity profiles among control and modified simulations are inconsistent with the changes in VGMS observed among the models, since the perturbed models with more top-heavy omega profiles have lower VGMS and stronger ISV. While the perturbed model versions are more bottom-heavy during suppressed precipitation periods, the control versions' tendency to become more bottom-heavy is greater.

To explain how VGMS could be reduced in the perturbed simulations even though the mean profiles are more top-heavy, starting from (1) we apply the following approximate partitioning:

$$\Delta\mathrm{VGMS} \approx -\frac{T_R\left\langle \Delta\omega\frac{\partial s}{\partial p}\right\rangle}{L\langle\nabla\cdot(r\mathbf{V})\rangle} - \frac{T_R\left\langle \omega\Delta\left(\frac{\partial s}{\partial p}\right)\right\rangle}{L\langle\nabla\cdot(r\mathbf{V})\rangle} - \frac{T_R\left\langle \Delta\omega\Delta\left(\frac{\partial s}{\partial p}\right)\right\rangle}{L\langle\nabla\cdot(r\mathbf{V})\rangle}, \tag{3}$$

where the delta operator represents the perturbed simulation minus the respective control, and all other variables represent those from the corresponding control simulations. This partitioning assumes that the changes in the numerator dominate VGMS changes among control and perturbed simulations for a given precipitation regime, a reasonable assumption based on sensitivity tests. The first term represents the VGMS change due to changes in the ω profile, the second term represents the change due to the MSE profile, and the third represents changes due to both the MSE and ω profiles. Variables averaged in the region 5°–20°N, 120°–90°W are used to calculate each term in the numerator of (3) and moisture convergence before computing the quotient during suppressed convective periods ($P_{30\text{–}90} < -0.5\sigma$), neutral periods ($|P_{30\text{–}90}| < 0.5\sigma$), and enhanced convective periods ($P_{30\text{–}90} > 0.5\sigma$). We define $P_{30\text{–}90}$ as the 30–90-day bandpass-filtered precipitation boreal summertime series for each model in the region 5°–20°N, 120°–90°W, and σ is its standard deviation. Table 2 shows the multimodel-ensemble mean of the three terms in (3), including a measure of multimodel spread as given by a 95% significance test using the t statistic. The gross behavior and sign of the change for each model pair is the same among all models for $-T_R\langle\Delta\omega(\partial s/\partial p)\rangle/L\langle\nabla\cdot(r\mathbf{V})\rangle$ and $-T_R\langle\omega\Delta(\partial s/\partial p)\rangle/L\langle\nabla\cdot(r\mathbf{V})\rangle$, except between SP-CAM and CAM during neutral periods where $-T_R\langle\Delta\omega(\partial s/\partial p)\rangle/L\langle\nabla\cdot(r\mathbf{V})\rangle$ reflects a modest decrease

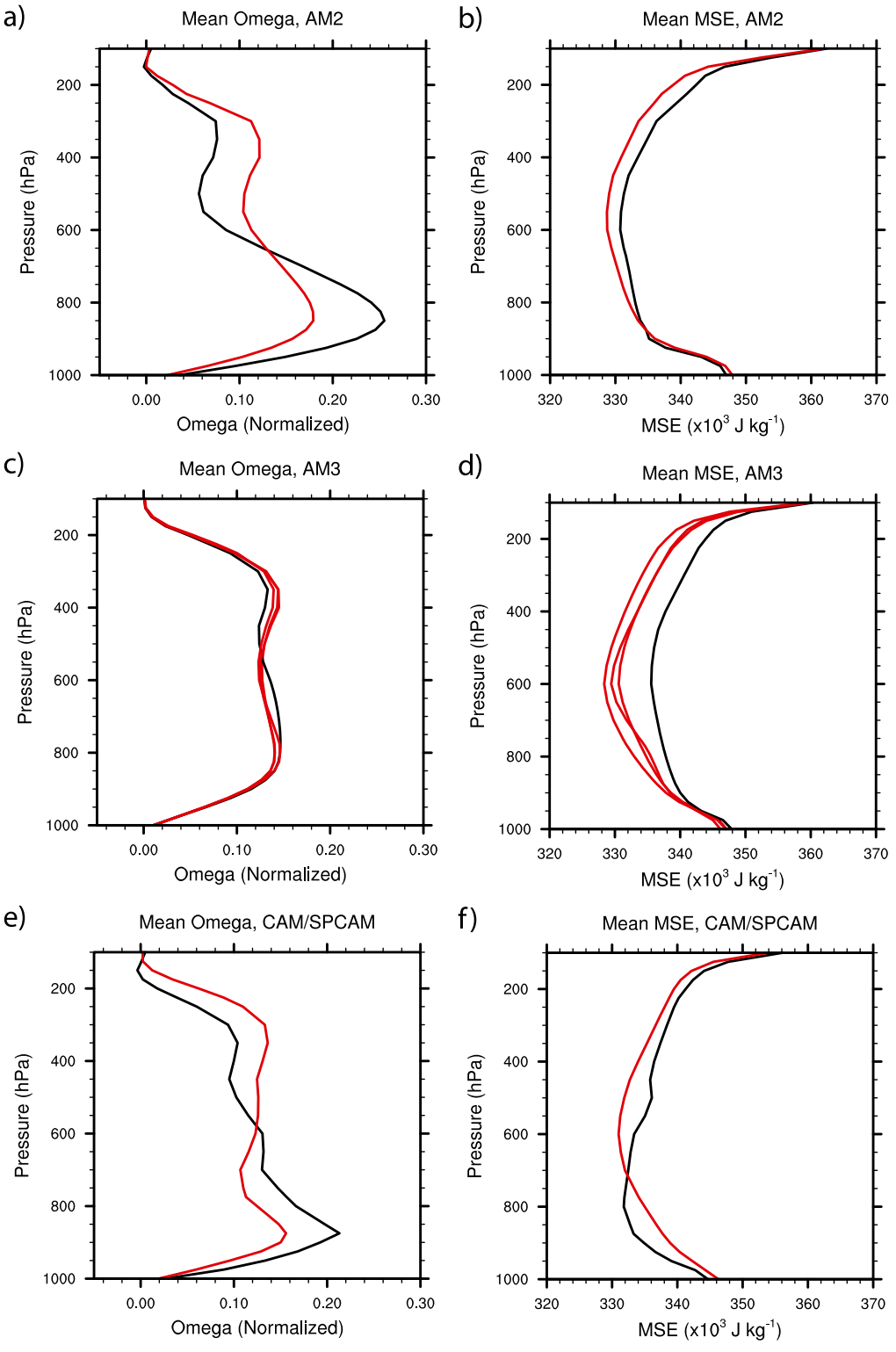

FIG. 10. Mean June–October ω profiles for (a) AM2, (c) AM3, and (e) CAM/SP-CAM; and MSE profiles for (b) AM2, (d) AM3, and (f) CAM/SP-CAM. Control model versions are in black and modified models are in red. Profiles are averaged in oceanic locations over the region 5°–20°N, 90°–120°W. The ω profiles have been normalized such that the mass weighted vertical integral = 1, which also changes the sign of these profiles relative to unnormalized values.

TABLE 2. Multimodel-ensemble mean partitioning of ΔVGMS. The 95% confidence intervals on the multimodel means are applied to provide a measure of model spread, with the mean values that are statistically significant from zero using the t statistic shown in bold.

	$-T_R\langle\Delta\omega(\partial s/\partial p)\rangle/L\langle\nabla\cdot(r\mathbf{V})\rangle$	$-T_R\langle\omega\Delta(\partial s/\partial p)\rangle/L\langle\nabla\cdot(r\mathbf{V})\rangle$	$-T_R\langle\Delta\omega\Delta(\partial s/\partial p)\rangle/L\langle\nabla\cdot(r\mathbf{V})\rangle$
Suppressed periods	**0.037 ± 0.033**	**−0.126 ± 0.080**	0.017 ± 0.029
Neutral periods	0.022 ± 0.035	**−0.097 ± 0.042**	0.001 ± 0.020
Enhanced periods	0.051 ± 0.058	**−0.070 ± 0.050**	−0.012 ± 0.024

of −0.01, compared to a larger magnitude change of −0.08 in $-T_R\langle\omega\Delta(\partial s/\partial p)\rangle/L\langle\nabla\cdot(r\mathbf{V})\rangle$ for this same model pair. Table 2 confirms that it is generally not the change in mean ω profile responsible for the lowering of VGMS in the perturbed simulations, but rather it is the change in the MSE or moist entropy profile, which dominates the VGMS changes in this simple calculation, especially during the suppressed and neutral periods.

The perturbed models with stronger ISV are characterized by a reduced MSE in the middle and upper troposphere relative to the control model, creating a more unstable atmospheric profile that would tend to lower GMS, consistent with the arguments of Frierson et al. (2011). The changes in MSE profiles in the upper troposphere are dominated by dry static energy changes, and those in the lower half of the troposphere are dominated by latent heat changes. Frierson et al. (2011) argue that convection schemes that are less active because of increased free tropospheric moisture sensitivity or other triggering conditions warm the upper troposphere less, reducing MSE there. Hannah and Maloney (2011) also argue that increased eddy activity in models with stronger moisture sensitivity can more effectively dry the lower and middle free troposphere, a result consistent with the increased HGMS in these models in Fig. 9b. The changes to the MSE profile are apparently more than enough to counteract the tendency of the mean ω profiles to be more top-heavy in the models with stronger ISV to produce lower VGMS. The CAM is a good demonstration of this behavior (Figs. 10e,f). Although the CAM ω profile is much more bottom-heavy than that of SP-CAM, the CAM vertical velocity maximum occurs in a region of near-zero vertical MSE gradient. As in Benedict et al. (2014), the CAM tends to produce a MSE minimum that occurs in the lower troposphere, below the midtropospheric MSE minimum that characterizes SP-CAM and observations (not shown). The vertical velocity maxima in control versions of AM2 and AM3 similarly occur in a region of weakened MSE gradient when compared to the perturbed simulations of the same models. The weakened lower tropospheric MSE gradient in the control simulations is generally consistent with the greater middle and upper tropospheric MSE in those simulations, although the lower tropospheric minimum in CAM also appears to have a strong contribution from the strong lower tropospheric dry bias present in CAM in this region (not shown here).

The tendency for the control models to have more bottom-heavy ω profiles than the perturbed models in which convective suppression is greater may deserve some discussion, as this is the opposite of the behavior seen in other studies. For example, Frierson et al. (2011) and Hannah and Maloney (2011) showed that making it more difficult for model deep convection to occur tends to create a more bottom-heavy vertical velocity profile in the Indo-Pacific warm pool. The region we analyze in this paper is somewhat unique in that it encompasses the east Pacific ITCZ, a region that is characterized by significant SST-driven boundary layer convergence and a resulting bottom-heavy vertical velocity profile (Back and Bretherton 2009a,b). The ERA-I omega profile (not shown here) actually looks very similar to that of AM2-TOK shown in red in Fig. 10a.

6. Conclusions

We have documented east Pacific ISV in eight atmospheric general circulation model simulations during June–October using a complex EOF (CEOF) analysis of 30–90-day precipitation. In addition to control versions of the GFDL AM2 and AM3 and the NCAR CAM, we also employed modified versions of these models in which deep convection is more difficult to trigger. The superparameterized CAM is the perturbed version of the NCAR CAM that is used in the comparison. We employed TRMM precipitation and ERA-I thermodynamic and dynamics fields as an observational comparison. Model leading mode amplitudes range from substantially stronger to substantially weaker than observed, with the modified models in which convection is more difficult to trigger demonstrating higher amplitude. Little correspondence is found between amplitude of the leading intraseasonal mode and fidelity at simulating observed propagation characteristics.

We then tested several process-oriented diagnostics to determine which of them could discriminate among models with strong and weak ISV, and also the ability to simulate observed propagation characteristics. The diagnostics tested were inspired by the hypothesis that ISV in the tropics is regulated by moisture mode theory

(e.g., Raymond et al. 2009). Diagnostics that were not able to discriminate the strength of ISV included the strength of the mean surface westerly flow in the warm pool, and the strength of the wind-induced surface flux feedback. Previous studies had suggested these diagnostics to be good discriminators of model tropical ISV (e.g., Rydbeck et al. 2013; Jiang et al. 2013; Maloney and Esbensen 2005), and so their lack of relationship with east Pacific ISV strength was somewhat surprising. We also find no relationship between the strength of ISV and average 500–850-hPa relative humidity for the top 1% of precipitation events. The strength of mean vertical shear of the zonal wind and strength of the mean 850-hPa zonal wind were not significantly related to success at simulating the observed propagation pattern, which is predominantly northward with a slight eastward component. We also tested whether coupling the SP-CAM to an ocean model could improve the representation of propagation, although found no significant difference in propagation characteristics (or amplitude) between coupled and uncoupled versions of SP-CAM.

We then presented two process-oriented diagnostics that are strongly related to amplitude of the leading intraseasonal mode. The difference in 500–850-hPa averaged relative humidity between the upper 5% and lower 10% of precipitation events shows a significant correlation with ISV amplitude (+0.7). This diagnostic is similar to one developed for the MJO by Kim et al. (2014). Models with greater spread in lower free tropospheric relative humidity between the top tier and bottom tier of precipitation events, consistent with greater convective sensitivity to environmental moisture, have stronger amplitude of the leading intraseasonal mode. An analysis of the June–October east Pacific warm pool moist entropy budget revealed a −0.9 correlation between the vertical component of gross moist stability (GMS) and leading mode amplitude, indicating that models in which convection and associated divergent circulations are on average less efficient at drying the column (or even contribute to moistening) support stronger ISV. These results are consistent with previous results for the MJO documented by Raymond and Fuchs (2009), Hannah and Maloney (2011), and Benedict et al. (2014). The horizontal component of GMS is significantly positively correlated with leading mode amplitude. One possible interpretation is that stronger ISV is associated with better organized intraseasonal horizontal flows that make moisture discharge by horizontal advection more efficient and also increased synoptic eddy activity that efficiently dries the east Pacific (e.g., Peters et al. 2008; Maloney 2009; Andersen and Kuang 2012). The time-mean omega profile in the east Pacific warm pool for the models with stronger intraseasonal amplitude is more top-heavy than for weaker simulations, suggesting that changes in the vertical profile of moist static energy (MSE) must be a strong driver of the lower vertical component of GMS in models with stronger ISV. This was verified by a partitioning of GMS. Models with stronger variability are accompanied by lower MSE in the middle to upper troposphere than corresponding control versions of models with weaker ISV, and a stronger lower tropospheric MSE gradient.

In moisture mode theory, it is effective GMS that is most important for destabilization of convective disturbances, where effective GMS includes the sum of the vertical GMS component plus radiative heating rate (Fuchs and Raymond 2002; Bretherton and Sobel 2002; Su et al. 2003; Kim et al. 2011a; Frierson et al. 2011). Surface fluxes can also be included to the extent that they are local to convection (Sugiyama 2009a,b; Maloney et al. 2010). We argued above that the strength of wind-induced flux feedbacks show no consistent relationship to the strength of ISV. Examining contributions to effective VGMS from radiative feedbacks will be a topic of future work, since previous studies have suggested cloud radiative feedbacks to be an important destabilization mechanism for ISV in other parts of the tropics (Bony and Emanuel 2005; Kim et al. 2011a; Andersen and Kuang 2012; Landu and Maloney 2011b). We also intend to extend this analysis to a broader set of models, to test whether the process-oriented diagnostics applied here are valid when considering greater diversity in base models.

Acknowledgments. Two reviewers provided excellent comments that led to significant improvements in the manuscript. The authors thank Cristiana Stan and Charlotte DeMott for making the SP-CCSM data available, and Mark Branson for help in running the CAM and SP-CAM simulations. This work was supported by the NOAA MAPP program under Grant NA12OAR4310077 (EDM and SPX) and NA12OAR4310075 (XJ), by the Climate and Large-Scale Dynamics Program of the National Science Foundation under Grants AGS-0946911, AGS-1025584 (EDM), and AGS-1228302 (XJ) and by the NASA CYGNSS program under Grant NNX13AQ50G (EDM). The statements, findings, conclusions, and recommendations do not necessarily reflect the views of NASA, NSF, NOAA, or the Department of Commerce.

REFERENCES

Andersen, J. A., and Z. Kuang, 2012: Moist static energy budget of MJO-like disturbances in the atmosphere of a zonally symmetric aquaplanet. *J. Climate,* **25,** 2782–2804, doi:10.1175/JCLI-D-11-00168.1.

Anderson, J. L., and Coauthors, 2004: The new GFDL global atmosphere and land model AM2–LM2: Evaluation with prescribed SST simulations. *J. Climate,* **17,** 4641–4673, doi:10.1175/JCLI-3223.1.

Back, L. E., and C. S. Bretherton, 2006: Geographic variability in the export of moist static energy and vertical motion profiles in the tropical Pacific. *Geophys. Res. Lett.,* **33,** L17810, doi:10.1029/2006GL026672.

——, and ——, 2009a: On the relationship between SST gradients, boundary layer winds, and convergence over the tropical oceans. *J. Climate,* **22,** 4182–4196, doi:10.1175/2009JCLI2392.1.

——, and ——, 2009b: A simple model of climatological rainfall and vertical motion patterns over the tropical oceans. *J. Climate,* **22,** 6477–6497, doi:10.1175/2009JCLI2393.1.

Barlow, M., and D. Salstein, 2006: Summertime influence of the Madden–Julian oscillation on daily rainfall over Mexico and Central America. *Geophys. Res. Lett.,* **33,** L21708, doi:10.1029/2006GL027738.

Barnett, T. P., 1983: Interaction of the monsoon and Pacific trade wind system at interannual time scales. Part I: The equatorial zone. *Mon. Wea. Rev.,* **111,** 756–773, doi:10.1175/1520-0493(1983)111<0756:IOTMAP>2.0.CO;2.

Bellon, G., A. H. Sobel, and J. Vialard, 2008: Ocean–atmosphere coupling in the monsoon intraseasonal oscillation: A simple model study. *J. Climate,* **21,** 5254–5270, doi:10.1175/2008JCLI2305.1.

Benedict, J. J., and D. A. Randall, 2009: Structure of the Madden–Julian oscillation in the superparameterized CAM. *J. Atmos. Sci.,* **66,** 3277–3296, doi:10.1175/2009JAS3030.1.

——, A. H. Sobel, E. D. Maloney, D. M. Frierson, and L. J. Donner, 2013: Tropical intraseasonal variability in version 3 of the GFDL Atmosphere Model. *J. Climate,* **26,** 426–449, doi:10.1175/JCLI-D-12-00103.1.

——, E. D. Maloney, A. H. Sobel, and D. M. W. Frierson, 2014: Gross moist stability and MJO simulation skill in three full-physics GCMs. *J. Atmos. Sci.,* doi:10.1175/JAS-D-13-0240.1, in press.

Bony, S., and K. A. Emanuel, 2005: On the role of moist processes in tropical intraseasonal variability: Cloud–radiation and moisture–convection feedbacks. *J. Atmos. Sci.,* **62,** 2770–2789, doi:10.1175/JAS3506.1.

Bretherton, C. S., and A. H. Sobel, 2002: A simple model of a convectively coupled Walker circulation using the weak temperature gradient approximation. *J. Climate,* **15,** 2907–2920, doi:10.1175/1520-0442(2002)015<2907:ASMOAC>2.0.CO;2.

——, M. E. Peters, and L. E. Back, 2004: Relationships between water vapor path and precipitation over the tropical oceans. *J. Climate,* **17,** 1517–1528, doi:10.1175/1520-0442(2004)017<1517:RBWVPA>2.0.CO;2.

Cai, Q., G. J. Zhang, and T. Zhou, 2013: Impacts of shallow convection on MJO simulation: A moist static energy and moisture budget analysis. *J. Climate,* **26,** 2417–2431, doi:10.1175/JCLI-D-12-00127.1.

Charney, J. G., 1963: A note on large-scale motions in the tropics. *J. Atmos. Sci.,* **20,** 607–609, doi:10.1175/1520-0469(1963)020<0607:ANOLSM>2.0.CO;2.

Collins, W. D., and Coauthors, 2006: The formulation and atmospheric simulation of the Community Atmosphere Model version 3 (CAM3). *J. Climate,* **19,** 2144–2161, doi:10.1175/JCLI3760.1.

Dee, D. P., and Coauthors, 2011: The ERA-Interim reanalysis: Configuration and performance of the data assimilation system. *Quart. J. Roy. Meteor. Soc.,* **137,** 553–597, doi:10.1002/qj.828.

DeMott, C. A., C. Stan, D. A. Randall, J. L. Kinter, and M. Khairoutdinov, 2011: The Asian monsoon in the superparameterized CCSM and its relationship to tropical wave activity. *J. Climate,* **24,** 5134–5156, doi:10.1175/2011JCLI4202.1.

Donner, L. J., and Coauthors, 2011: The dynamical core, physical parameterizations, and basic simulation characteristics of the atmospheric component AM3 of the GFDL global coupled model CM3. *J. Climate,* **24,** 3484–3519, doi:10.1175/2011JCLI3955.1.

Frierson, D. M. W., D. Kim, I.-S. Kang, M.-I. Lee, and J. Lin, 2011: Structure of AGCM-simulated convectively coupled Kelvin waves and sensitivity to convective parameterization. *J. Atmos. Sci.,* **68,** 26–45, doi:10.1175/2010JAS3356.1.

Fu, X., and B. Wang, 2004: Differences of boreal summer intraseasonal oscillations simulated in an atmosphere–ocean coupled model and an atmosphere-only model. *J. Climate,* **17,** 1263–1271, doi:10.1175/1520-0442(2004)017<1263:DOBSIO>2.0.CO;2.

Fuchs, Ž., and D. J. Raymond, 2002: Large-scale modes of a nonrotating atmosphere with water vapor and cloud–radiation feedbacks. *J. Atmos. Sci.,* **59,** 1669–1679, doi:10.1175/1520-0469(2002)059<1669:LSMOAN>2.0.CO;2.

Hannah, W. M., and E. D. Maloney, 2011: The role of moisture–convection feedbacks in simulating the Madden–Julian oscillation. *J. Climate,* **24,** 2754–2770, doi:10.1175/2011JCLI3803.1.

Horel, J. D., 1984: Complex principal component analysis: Theory and examples. *J. Climate Appl. Meteor.,* **23,** 1660–1673, doi:10.1175/1520-0450(1984)023<1660:CPCATA>2.0.CO;2.

Huffman, G. J., and Coauthors, 2007: The TRMM Multisatellite Precipitation Analysis (TMPA): Quasi-global, multiyear, combined-sensor precipitation estimates at fine scales. *J. Hydrometeor.,* **8,** 38–55, doi:10.1175/JHM560.1.

Jiang, X., and D. E. Waliser, 2008: Northward propagation of the subseasonal variability over the eastern Pacific warm pool. *Geophys. Res. Lett.,* **35,** L09814, doi:10.1029/2008GL033723.

——, and ——, 2009: Two dominant subseasonal variability modes of the eastern Pacific ITCZ. *Geophys. Res. Lett.,* **36,** L04704, doi:10.1029/2008GL036820.

——, and Coauthors, 2012: Simulation of the intraseasonal variability over the eastern Pacific ITCZ in climate models. *Climate Dyn.,* **39,** 617–636, doi:10.1007/s00382-011-1098-x.

——, E. D. Maloney, J.-L. F. Li, and D. E. Waliser, 2013: Simulations of the eastern North Pacific intraseasonal variability in CMIP5 GCMs. *J. Climate,* **26,** 3489–3510, doi:10.1175/JCLI-D-12-00526.1.

Khairoutdinov, M., C. DeMott, and D. Randall, 2008: Evaluation of the simulated interannual and subseasonal variability in an AMIP-style simulation using the CSU Multiscale Modeling Framework. *J. Climate,* **21,** 413–431, doi:10.1175/2007JCLI1630.1.

Kim, D., A. H. Sobel, and I.-S. Kang, 2011a: A mechanism denial study on the Madden–Julian oscillation. *J. Adv. Model. Earth Syst.,* **3,** M12007, doi:10.1029/2011MS000081.

——, ——, E. D. Maloney, D. M. W. Frierson, and I.-S. Kang, 2011b: A systematic relationship between intraseasonal variability and mean state bias in AGCM simulations. *J. Climate,* **24,** 5506–5520, doi:10.1175/2011JCLI4177.1.

——, and Coauthors, 2014: Process-oriented MJO simulation diagnostic: Moisture sensitivity of simulated convection. *J. Climate,* **27,** 5379–5395, doi:10.1175/JCLI-D-13-00497.1.

Klingaman, N. P., P. M. Inness, H. Weller, and J. M. Slingo, 2008: The importance of high-frequency sea surface temperature variability to the intraseasonal oscillation of Indian

monsoon rainfall. *J. Climate,* **21,** 6119–6140, doi:10.1175/2008JCLI2329.1.

Landu, K., and E. D. Maloney, 2011a: Intraseasonal moist static energy budget in reanalysis data. *J. Geophys. Res.,* **116,** D21117, doi:10.1029/2011JD016031.

——, and ——, 2011b: Effect of SST distribution and radiative feedbacks on the simulation of intraseasonal variability in an aquaplanet GCM. *J. Meteor. Soc. Japan,* **89,** 195–210, doi:10.2151/jmsj.2011-302.

Lin, J.-L., B. E. Mapes, K. M. Weickmann, G. N. Kiladis, S. D. Schubert, M. J. Suarez, J. T. Bacmeister, and M.-I. Lee, 2008: North American monsoon and convectively coupled equatorial waves simulated by IPCC AR4 coupled GCMs. *J. Climate,* **21,** 2919–2937, doi:10.1175/2007JCLI1815.1.

Madden, R., and P. R. Julian, 2005: Historical perspective. *Intraseasonal Variability in the Atmosphere–Ocean Climate System,* W. K. M. Lau and D. E. Waliser, Eds., Springer, 1–18.

Maloney, E. D., 2009: The moist static energy budget of a composite tropical intraseasonal oscillation in a climate model. *J. Climate,* **22,** 711–729, doi:10.1175/2008JCLI2542.1.

——, and D. L. Hartmann, 2000a: Modulation of eastern North Pacific hurricanes by the Madden–Julian oscillation. *J. Climate,* **13,** 1451–1460, doi:10.1175/1520-0442(2000)013<1451:MOENPH>2.0.CO;2.

——, and ——, 2000b: Modulation of hurricane activity in the Gulf of Mexico by the Madden–Julian oscillation. *Science,* **287,** 2002–2004, doi:10.1126/science.287.5460.2002.

——, and J. T. Kiehl, 2002: Intraseasonal eastern Pacific precipitation and SST variations in a GCM coupled to a slab ocean model. *J. Climate,* **15,** 2989–3007, doi:10.1175/1520-0442(2002)015<2989:IEPPAS>2.0.CO;2.

——, and S. K. Esbensen, 2003: The amplification of east Pacific Madden–Julian oscillation convection and wind anomalies during June–November. *J. Climate,* **16,** 3482–3497, doi:10.1175/1520-0442(2003)016<3482:TAOEPM>2.0.CO;2.

——, and A. H. Sobel, 2004: Surface fluxes and ocean coupling in the tropical intraseasonal oscillation. *J. Climate,* **17,** 4368–4386, doi:10.1175/JCLI-3212.1.

——, and S. K. Esbensen, 2005: A modeling study of summertime east Pacific wind-induced ocean–atmosphere exchange in the intraseasonal oscillation. *J. Climate,* **18,** 568–584, doi:10.1175/JCLI-3280.1.

——, and ——, 2007: Satellite and buoy observations of boreal summer intraseasonal variability in the tropical northeast Pacific. *Mon. Wea. Rev.,* **135,** 3–19, doi:10.1175/MWR3271.1.

——, and S.-P. Xie, 2013: Sensitivity of tropical intraseasonal variability to the pattern of climate warming. *J. Adv. Model. Earth Syst.,* **5,** 32–47, doi:10.1029/2012MS000171.

——, D. B. Chelton, and S. K. Esbensen, 2008: Subseasonal SST variability in the tropical eastern North Pacific during boreal summer. *J. Climate,* **21,** 4149–4167, doi:10.1175/2007JCLI1856.1.

——, A. H. Sobel, and W. M. Hannah, 2010: Intraseasonal variability in an aquaplanet general circulation model. *J. Adv. Model. Earth. Syst.,* **2,** 5, doi:10.3894/JAMES.2010.2.5.

Mapes, B. E., and J. T. Bacmeister, 2012: Diagnosis of tropical biases and the MJO from patterns in the MERRA analysis tendency fields. *J. Climate,* **25,** 6202–6214, doi:10.1175/JCLI-D-11-00424.1.

Neelin, J. D., and I. M. Held, 1987: Modeling tropical convergence based on the moist static energy budget. *Mon. Wea. Rev.,* **115,** 3–12, doi:10.1175/1520-0493(1987)115<0003:MTCBOT>2.0.CO;2.

Peters, M. E., and C. S. Bretherton, 2006: Structure of tropical variability from a vertical mode perspective. *Theor. Comput. Fluid. Dyn.,* **20,** 501–524, doi:10.1007/s00162-006-0034-x.

——, Z. Kuang, and C. C. Walker, 2008: Analysis of atmospheric energy transport in ERA-40 and implications for simple models of the mean tropical circulation. *J. Climate,* **21,** 5229–5241, doi:10.1175/2008JCLI2073.1.

Pritchard, M. S., and C. S. Bretherton, 2014: Causal evidence that rotational moisture advection is critical to the superparameterized Madden–Julian oscillation. *J. Atmos. Sci.,* **71,** 800–815, doi:10.1175/JAS-D-13-0119.1.

Randall, D., M. Khairoutdinov, A. Arakawa, and W. Grabowski, 2003: Breaking the cloud parameterization deadlock. *Bull. Amer. Meteor. Soc.,* **84,** 1547–1564, doi:10.1175/BAMS-84-11-1547.

Raymond, D. J., 2001: A new model of the Madden–Julian oscillation. *J. Atmos. Sci.,* **58,** 2807–2819, doi:10.1175/1520-0469(2001)058<2807:ANMOTM>2.0.CO;2.

——, and Z. Fuchs, 2009: Moisture modes and the Madden–Julian oscillation. *J. Climate,* **22,** 3031–3046, doi:10.1175/2008JCLI2739.1.

——, S. Sessions, A. H. Sobel, and Ž. Fuchs, 2009: The mechanics of gross moist stability. *J. Adv. Model. Earth Syst.,* **1,** 9, doi:10.3894/JAMES.2009.1.9.

Rydbeck, A. V., E. D. Maloney, S.-P. Xie, J. Hafner, and J. Shaman, 2013: Remote forcing versus local feedback of east Pacific intraseasonal variability during boreal summer. *J. Climate,* **26,** 3575–3596, doi:10.1175/JCLI-D-12-00499.1.

Sahany, S., J. D. Neelin, K. Hales, and R. B. Neale, 2012: Temperature–moisture dependence of the deep convective transition as a constraint on entrainment in climate models. *J. Atmos. Sci.,* **69,** 1340–1358, doi:10.1175/JAS-D-11-0164.1.

Sharmila, S., and Coauthors, 2013: Role of ocean–atmosphere interaction on northward propagation of Indian summer monsoon intra-seasonal oscillations (MISO). *Climate Dyn.,* **41,** 1651–1669, doi:10.1007/s00382-013-1854-1.

Small, R. J., S.-P. Xie, E. D. Maloney, S. P. de Szoeke, and T. Miyama, 2011: Intraseasonal variability in the far-east Pacific: Investigation of the role of air–sea coupling in a regional coupled model. *Climate Dyn.,* **36,** 867–890, doi:10.1007/s00382-010-0786-2.

Sobel, A. H., and E. D. Maloney, 2013: Moisture modes and the eastward propagation of the MJO. *J. Atmos. Sci.,* **70,** 187–192, doi:10.1175/JAS-D-12-0189.1.

——, J. Nilsson, and L. M. Polvani, 2001: The weak temperature gradient approximation and balanced tropical moisture waves. *J. Atmos. Sci.,* **58,** 3650–3665, doi:10.1175/1520-0469(2001)058<3650:TWTGAA>2.0.CO;2.

——, E. D. Maloney, G. Bellon, and D. M. Frierson, 2010: Surface fluxes and tropical intraseasonal variability: A reassessment. *J. Adv. Model. Earth Syst.,* **2,** 2, doi:10.3894/JAMES.2010.2.2.

Stan, C., M. Khairoutdinov, C. A. DeMott, V. Krishnamurthy, D. M. Straus, D. A. Randall, J. L. Kinter III, and J. Shukla, 2010: An ocean–atmosphere climate simulation with an embedded cloud resolving model. *Geophys. Res. Lett.,* **37,** L01702, doi:10.1029/2009GL040822.

Su, H., J. D. Neelin, and J. E. Meyerson, 2003: Sensitivity of tropical tropospheric temperature to sea surface temperature forcing. *J. Climate,* **16,** 1283–1301, doi:10.1175/1520-0442-16.9.1283.

Sugiyama, M., 2009a: The moisture mode in the quasi-equilibrium tropical circulation model. Part I: Analysis based on the weak temperature gradient approximation. *J. Atmos. Sci.,* **66,** 1507–1523, doi:10.1175/2008JAS2690.1.

——, 2009b: The moisture mode in the quasi-equilibrium tropical circulation model. Part II: Nonlinear behavior on an

equatorial β plane. *J. Atmos. Sci.,* **66,** 1525–1542, doi:10.1175/2008JAS2691.1.

Thayer-Calder, K., and D. A. Randall, 2009: The role of convective moistening in the Madden–Julian oscillation. *J. Atmos. Sci.,* **66,** 3297–3312, doi:10.1175/2009JAS3081.1.

Tokioka, T., K. Yamazaki, A. Kitoh, and T. Ose, 1988: The equatorial 30–60 day oscillation and the Arakawa–Schubert penetrative cumulus parameterization. *J. Meteor. Soc. Japan,* **66,** 883–901.

Van Roekel, L. P., and E. D. Maloney, 2012: Mixed layer modeling in the east Pacific warm pool during 2002. *Climate Dyn.,* **38,** 2559–2573, doi:10.1007/s00382-011-1130-1.

Wang, W., M. Chen, and A. Kumar, 2009: Impacts of ocean surface on the northward propagation of the boreal summer intraseasonal oscillation in the NCEP Climate Forecast System. *J. Climate,* **22,** 6561–6576, doi:10.1175/2009JCLI3007.1.

Wen, M., S. Yang, W. Higgins, and R. Zhang, 2011: Characteristics of the dominant modes of atmospheric quasi-biweekly oscillation over tropical–subtropical Americas. *J. Climate,* **24,** 3956–3970, doi:10.1175/2011JCLI3916.1.

Wheeler, M. W., and Coauthors, 2013: Madden–Julian oscillation (MJO) Task Force: A joint effort of the climate and weather communities. *CLIVAR Exchanges,* No. 61, International CLIVAR Project Office, Southampton, United Kingdom, 3–5.

Yano, J.-I., and M. Bonazzola, 2009: Scale analysis for large-scale tropical atmospheric dynamics. *J. Atmos. Sci.,* **66,** 159–172, doi:10.1175/2008JAS2687.1.

Zhang, C., J. Gottschalck, E. Maloney, M. Moncrieff, F. Vitart, D. Waliser, B. Wang, and M. Wheeler, 2013: Cracking the MJO nut. *Geophys. Res. Lett.,* **40,** 1223–1230, doi:10.1002/grl.50244.

Zhang, G. J., 2002: Convective quasi-equilibrium in midlatitude continental environment and its effect on convective parameterization. *J. Geophys. Res.,* **107,** 4220, doi:10.1029/2001JD001005.

——, and N. A. McFarlane, 1995: Sensitivity of climate simulations to the parameterization of cumulus convection in the Canadian Climate Centre general circulation model. *Atmos.–Ocean,* **33,** 407–446, doi:10.1080/07055900.1995.9649539.

Zhu, H., H. Hendon, and C. Jakob, 2009: Convection in a parameterized and superparameterized model and its role in the representation of the MJO. *J. Atmos. Sci.,* **66,** 2796–2811, doi:10.1175/2009JAS3097.1.